

Nuclei embedded in an electron gas

Thomas J. Bürvenich,^{*} Igor N. Mishustin,[†] and Walter Greiner[‡]

Frankfurt Institute for Advanced Studies,

Johann Wolfgang Goethe University, Max-von-Laue-Str. 1,

60438 Frankfurt am Main, Germany

(Dated: August 10, 2021)

Abstract

The properties of nuclei embedded in an electron gas are studied within the relativistic mean-field approach. These studies are relevant for nuclear properties in astrophysical environments such as neutron-star crusts and supernova explosions. The electron gas is treated as a constant background in the Wigner-Seitz cell approximation. We investigate the stability of nuclei with respect to α and β decay. Furthermore, the influence of the electronic background on spontaneous fission of heavy and superheavy nuclei is analyzed. We find that the presence of the electrons leads to stabilizing effects for both α decay and spontaneous fission for high electron densities. Furthermore, the screening effect shifts the proton dripline to more proton-rich nuclei, and the stability line with respect to β -decay is shifted to more neutron-rich nuclei. Implications for the creation and survival of very heavy nuclear systems are discussed.

PACS numbers: 21.10.Dr, 21.10.Ft, 21.10.Tg, 23.60.+e, 26.50.+x,

^{*}Electronic address: buervenich@fias.uni-frankfurt.de

[†]Electronic address: mishustin@fias.uni-frankfurt.de

[‡]Electronic address: greiner@fias.uni-frankfurt.de

I. INTRODUCTION

Nuclear astrophysics lies at the heart of understanding the origin of the physical world and our mere existence. One of its key questions is 'How and where did the chemical elements originate?'. Many challenging questions concerning the processes and mechanisms for nucleosynthesis are in the focus of modern research. In this respect, supernovae and neutron stars are the most interesting objects to study.

The first attempt to explain abundances of chemical elements in the solar system was made by Geoge Gamow in 1946-48 (see e.g. Ref. [1]). He proposed a mechanism that was based on a continuous building-up of chemical elements by neutron capture in the early universe. Later it became clear that this mechanism cannot explain the production of heavy elements because of very high specific entropy of the early universe, $S/B \sim 10^{10}$, where S is the total entropy and B is the net baryon number. The present understanding of the element creation says that the lightest elements (up to He, and, partly, Li) were formed during the first moments of the universe expansion, immediately after the Big Bang. Heavier elements up to oxygen are predominantly produced in thermonuclear reactions in stars like our Sun. Elements up to iron and nickel could be produced in more massive stars. The origin of heavier elements such as gold and uranium remains in the focus of current research. It is widely believed that heavy elements were mostly synthesized in the course of supernova explosions in the so-called r-process (subsequent neutron capture by stable and unstable nuclei, see a recent review [2]).

A type II supernova explosion is one of the most spectacular events in astrophysics, with huge energy release of about 10^{53} erg or several tens of MeV per nucleon [3]. When the core of a massive star collapses, it reaches densities several times larger than the normal nuclear density $\rho_0 = 0.16 \text{ fm}^{-3}$. The repulsive nucleon-nucleon interaction gives rise to a bounce-off of matter and formation of a shock wave propagating through the in-falling stellar material, predominantly Fe.

Hydrodynamical simulations (see e.g. Refs. [4, 5]) show that during the collapse and subsequent explosion the temperatures $T \approx (0.5 \div 10) \text{ MeV}$ and baryon densities $\rho_B \approx (10^{-5} \div 2)\rho_0$ can be reached. Unfortunately, these simulations do not produce successful explosions yet, even when neutrino heating and convection effects are included. This means that some important physics of this process is still missing.

Besides supernova explosions, proto-neutron and neutron stars are interesting objects from a nuclear physics point of view. They are quite similar to huge, extremely neutron-rich macroscopic nuclei that gain additional stability and binding due to the gravitational force. Neutron stars are very compact objects with a central density of about $\rho = 10^{15} \text{g/cm}^3$, a typical radius of $R = 10 \text{ km}$ and masses up to 2 solar-masses. Proto-neutron stars are newly-born neutron stars formed in the course of a supernova explosion. They are somewhat bigger than neutron stars and have temperatures up to 30 MeV. The regime of interest for our considerations are baryon densities in the range $0.001 - 0.5\rho_0$, where very heavy and neutron-rich nuclei may be present [6, 7, 8, 9]. Nuclear pasta phases, i.e., nuclear matter in various geometries such as slabs and parallel plates, reminiscent of *pasta* [10, 11, 12, 13] start at densities slightly above $0.5 \rho_0$. In this regime the neutrons need to be taken into account.

Since the heaviest elements occurring in nature are Uranium isotopes, there should have been corresponding extreme conditions for their creation and persistence, in supernova explosions, crusts of neutron stars, or other sites. Thus we may wonder if very heavy and superheavy systems can and will be produced under such conditions too. How are the properties of such nuclear systems altered in dense environments?

The properties of nuclei in astrophysical environments have enjoyed continuous interest for over more than 30 years. The seminal work by Negele and Vautherin [14] layed out the path for microscopic studies of nuclei in stellar environments, see e.g. Refs. [8, 12, 13, 15, 16, 17, 18, 19, 20]. The investigation of the rich properties of nuclear systems under extreme conditions in astrophysical environments is on the rising path. Since many astrophysical calculations, from r-process to dynamical simulations of supernova explosions, depend on theoretical nuclear input, it is important to understand how nuclei subject to these special conditions differ from nuclei studied in the laboratory on earth.

In this paper we focus on the physics of nuclei embedded in a dense electron gas. This investigation is important by itself as well as for further studies including the neutron gas. We consider nuclei across the periodic chart up to superheavy nuclei embedded in a Wigner-Seitz cell with constant electron density. The presence of the electrons will effect the location of the β -stability line and the proton dripline as well as decay modes such as α -decay and spontaneous fission.

The paper is structured as follows: In Section II, we present the relativistic mean-field

model which is employed in the calculations as well as the concept of the Wigner-Seitz cell and its concrete implementation for spherical and deformed nuclear systems. In Section III, we discuss the β -equilibrium condition and present results for the β -stability line and the proton and neutron drip lines in the presence of electrons. The evolution of the α -decay mode in heavy nuclei as a function of the electron Fermi momentum is demonstrated in Section IV A. In Section IV B, deformed nuclei are considered and spontaneous fission under the influence of the electron background is studied. Finally, in Section V we conclude and give an outline of future research directions.

II. THE FRAMEWORK

A. The RMF model

Over the years self-consistent mean-field models have reached high predictive power. They can be applied from medium-light systems up to superheavy nuclei and to systems ranging from the proton drip line to the neutron drip line. They are based on the formulation of an effective nucleon-nucleon interaction meant to be employed in the Hartree or Hartree-Fock treatment of nuclear systems. The modern way of formulating them is in terms of an energy functional that can incorporate terms which can not be constructed via a two- (or three- or four-) body force.

In this paper we employ the relativistic mean-field (RMF) model [21, 22]. The effective in-medium nucleon-nucleon interaction is parametrized via the exchange of several meson fields: scalar-isoscalar (σ), vector-isovector (ω_μ) and vector-isovector ($\vec{\rho}_\mu$).

This model is based on an effective Lagrangian of the form

$$\begin{aligned}
\mathcal{L} = & \sum_{\alpha} w_{\alpha} \bar{\psi}_{\alpha} (i\gamma_{\mu} \partial^{\mu} - m_N) \psi \\
& + \frac{1}{2} \partial_{\nu} \sigma \partial^{\nu} \sigma - \frac{1}{2} m_{\sigma}^2 \sigma^2 - \frac{b}{3} \sigma^3 - \frac{c}{4} \sigma^4 - g_{\sigma} \sum_{\alpha} w_{\alpha} \sigma \bar{\psi}_{\alpha} \psi_{\alpha} \\
& - \frac{1}{4} \omega_{\mu\nu} \omega^{\mu\nu} - \frac{1}{2} m_{\omega}^2 \omega^{\mu} \omega_{\mu} - g_{\omega} \sum_{\alpha} w_{\alpha} \omega^{\mu} \bar{\psi}_{\alpha} \gamma_{\mu} \psi_{\alpha} \\
& - \frac{1}{4} \vec{\rho}_{\mu\nu} \cdot \vec{\rho}^{\mu\nu} - \frac{1}{2} m_{\rho}^2 \vec{\rho}^{\mu} \cdot \vec{\rho}_{\mu} - g_{\rho} \sum_{\alpha} w_{\alpha} \vec{\rho}^{\mu} \cdot \bar{\psi}_{\alpha} \gamma_{\mu} \vec{\tau} \psi_{\alpha} \\
& - \frac{1}{4} F_{\mu\nu} F^{\mu\nu} - e \sum_{\alpha} w_{\alpha} A^{\mu} \bar{\psi}_{\alpha} \gamma_{\mu} \frac{1 + \tau_3}{2} \psi_{\alpha}
\end{aligned} \tag{2.1}$$

The field tensor for the ω meson is defined as $\omega_{\mu\nu} = \partial_\mu\omega_\nu - \partial_\nu\omega_\mu$, and similar definitions hold for the field tensors of the ρ meson and the photon. The parameters $g_\sigma, g_\omega, g_\rho, m_\sigma, b, c$ are fitted to experimental data of nuclear ground-state observables. The masses of the ρ and ω mesons are fixed at the experimental values, since the performance of the model is not quite sensitive to their values. As it is written down in the Hartree approximation, the meson fields are treated as classical potentials and the nucleons are represented by Dirac spinors. The isoscalar-scalar σ meson delivers the intermediate-range attraction, while the isoscalar-vector ω meson is responsible for the short-range repulsion. The isovector-vector ρ meson couples to the isovector nucleon density and thus parametrizes the isovector properties of the model. The photon is coupled in standard fashion. For all boson fields, no (explicit) exchange terms are taken into account.

It is worth mentioning that these meson fields have only loose correspondence with the physical meson spectrum. Mean-field models employing contact interactions between nucleons have a comparable predictive power for nuclear ground-state observables and excited states [23, 24, 25].

The w_α denote occupation probabilities of the nucleon states and originate from the treatment of pairing. We employ BCS pairing with a density-independent δ -force, see Ref. [26] for details. In time-reversal even-even systems, only the time components of the vector mesons are non-zero. Proton and neutron states are not allowed to mix, hence only the third components of the isovector-vector ρ field associated with τ_3 survives.

The single-particle equation for the nucleons reads

$$[i\vec{\gamma} \cdot \vec{\partial} + m_N + g_\sigma\sigma + g_\omega\omega^0\gamma_0 + g_\rho\rho_3^0\tau_3 + eA^0\frac{1-\tau_3}{2}\gamma_0]\psi = \epsilon\gamma_0\psi \quad (2.2)$$

The binding properties of nuclear matter and nuclei are generated from the strong scalar and vector fields, $U_S = g_\sigma\sigma \approx -350$ MeV, $U_V = g_\omega\omega^0 \approx +300$ MeV, which add up to a normal nucleon potential $U_N = U_S + U_V \approx -50$ MeV. They add up with the same sign to generate the strong spin-orbit potential in nuclei, which (in the nonrelativistic limit) is given by

$$V_{ls} \propto \frac{d}{dr}(V_S - V_V\gamma_0)\vec{l} \cdot \vec{s} \quad (2.3)$$

This spin-orbit force emerges from the covariant formalism with the right sign and magnitude without introducing additional parameters. This is an important consequence of the relativistic description.

In order to account for the electron background, we modify the source term of the photon field by adding the electron density, i.e.

$$\Delta\phi = -e(\rho_p - \rho_e) = -e\rho_{ch}, \quad (2.4)$$

which is the Poisson equation for the electrostatic potential $\phi \equiv A_0$. Further down we discuss the concrete implementation in different symmetries. All other equations remain the same as in vacuum.

Calculations are performed in coordinate space, but the derivatives are performed as matrix multiplications in Fourier space. We employ the mean-field parametrization NL3 in these studies [27] which delivers accurate values for nuclear ground-state properties. Furthermore, since the external electron background couples only electromagnetically to nucleons, no additional parameters need to be introduced, and no readjustment of the present parameters is needed.

B. The Wigner-Seitz approximation

In this paper we study properties of nuclei embedded in a uniform electron gas at zero temperature. The calculations are performed within the Wigner-Seitz (WS) approximation by dividing the system into WS cells, each containing only one nucleus and the number of electrons equal to the nuclear charge Z , see Fig. 1 for an illustration.

The construction of the WS cell is aimed at an approximate and convenient segmentation of an ensemble of nuclei surrounded by the uniform background of electrons. Its construction should ensure that the physics contained in the Wigner-Seitz cell is to an optimally large degree isolated from the surrounding. This requires, for example, charge neutrality of the cell. However, there could be also other requirements which minimize the electrostatic interactions with neighbouring cells (see below). Recently the validity of the WS approximation for the inner neutron-star crust has been discussed, e. g. in Ref. [28].

At electron densities considered in this work, the Coulomb potential due to the nucleus is a small perturbation compared to the Fermi energy of the electrons. Thus the electrons will only be weakly affected by the presence of the nucleus which justifies the approximation of constant density.

In the numerical implementation, however, we use a Fermi-type distribution of the elec-

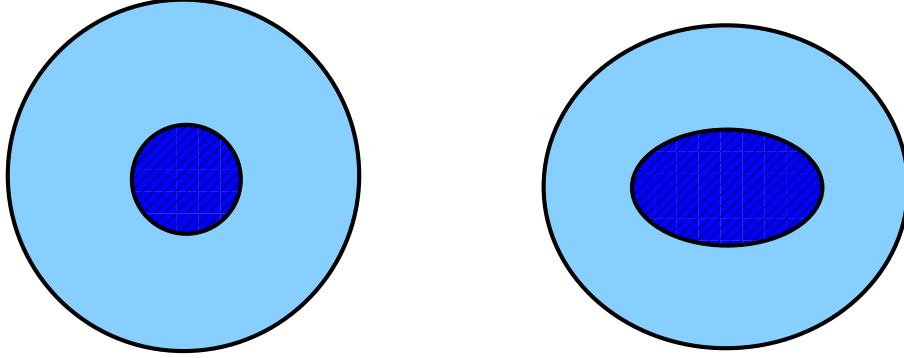


FIG. 1: (COLOR ONLINE): Illustration of a Wigner Seitz cell for a spherical nucleus (left) and an axially deformed nucleus (right). The inner dark filled region denotes the charge density of the nucleus, the outer region denotes the extension of the electron background surrounding the nucleus. The figure is not to scale.

tron density with a smooth boundary. The reason is that on a spherical grid in coordinate space, the cell radius cannot be fixed exactly (it is limited to any value that is a multiple of the grid spacing Δr). A smooth surface region allows us to realize the electron shell for any grid spacing and radius. The parameters of the shell are chosen to satisfy the charge neutrality condition $\int dV \rho_{ch}(\vec{r}) = 0$, where $\rho_{ch}(\vec{r})$ is the total charge density. Since in the computer code the derivatives are calculated in Fourier space, the numerical realization of the smooth surface region is not very sensitive to the chosen grid-spacing. This construction of the electron density allows us to calculate nuclei throughout the nuclear chart without introducing artificial jumps in the energy caused by a step-like change of the WS cell radius.

1. The spherical cell

For a given nuclear charge Z the WS cell radius R_C is uniquely determined by the charge neutrality requirement

$$\frac{4\pi}{3} R_C^3 \rho_e = Z \quad (2.5)$$

Expressing the electron density in terms of the electron Fermi momentum k_F , $\rho_e = \frac{1}{3\pi^2} k_F^3$, one can write the cell radius as

$$R_C = \left(\frac{9\pi Z}{4} \right)^{1/3} \frac{1}{k_F} \quad (2.6)$$

The parametrization with a smooth surface, as used in this work, is given by

$$\rho_e(r) = \frac{\rho_{e0}}{1 + \exp\left(\frac{r-r_C}{a}\right)}, \quad (2.7)$$

where ρ_{e0} is the background electron density, r_C is adjusted in order to fulfill charge neutrality, and a is the diffuseness parameter of the distribution, taken to be 0.45 fm. The parameter a is chosen such that the charge density is dropping from 90% to 10% of its value at $r = 0$ within the diffuseness interval $\sigma = 4.4 * a = 2$ fm. We have checked that the results, in particular the differences of nuclear binding energies, are not sensitive to the choice of a . The Poisson equation (2.4) has to be solved numerically.

While these calculations can be performed quite easily for high electron densities, for low electron densities when the WS cell radius becomes quite large, numerical problems arise. For example, for a tin nucleus, at $k_F = 0.1$ fm⁻¹, the WS cell radius is $R_C \approx 70$ fm, while for $k_F = 0.01$ fm⁻¹ it corresponds to $R_C \approx 700$ fm.

An alternative way of calculating the effect of the electron gas is to add the potential of a homogeneously charged sphere of electrons to the electric potential of the proton charge distribution, i.e., first calculate the proton electric potential,

$$\Delta\phi_p = -e\rho_p \quad (2.8)$$

then add the potential due to electrons,

$$\phi = \phi_p + \phi_e \quad (2.9)$$

where ϕ_p is the solution of the Poisson equation for the proton charge density. The electric potential caused by the uniform background of electrons reads

$$\phi_e(r) = \begin{cases} \frac{-Ze}{4\pi R_C} \left[\frac{3}{2} - \frac{1}{2} \frac{r^2}{R_C^2} \right], & r < R_C \\ \frac{-Ze}{4\pi r}, & r \geq R_C \end{cases} \quad (2.10)$$

As can be seen from Fig. 2, the two different ways of calculating the total electric potential, Eq. (2.4) and Eq. (2.9), lead to identical electric potentials (apart from the correction due to the smooth surface region in Eq. (2.4)) and, therefore, to the same structure of the nucleus. This demonstrates consistency and accuracy of the treatment of the electron background in our numerical calculations.

It is clear that the total energy of the cell should include the interaction energy of the electrons with the electromagnetic field, which does not appear when the electrons are

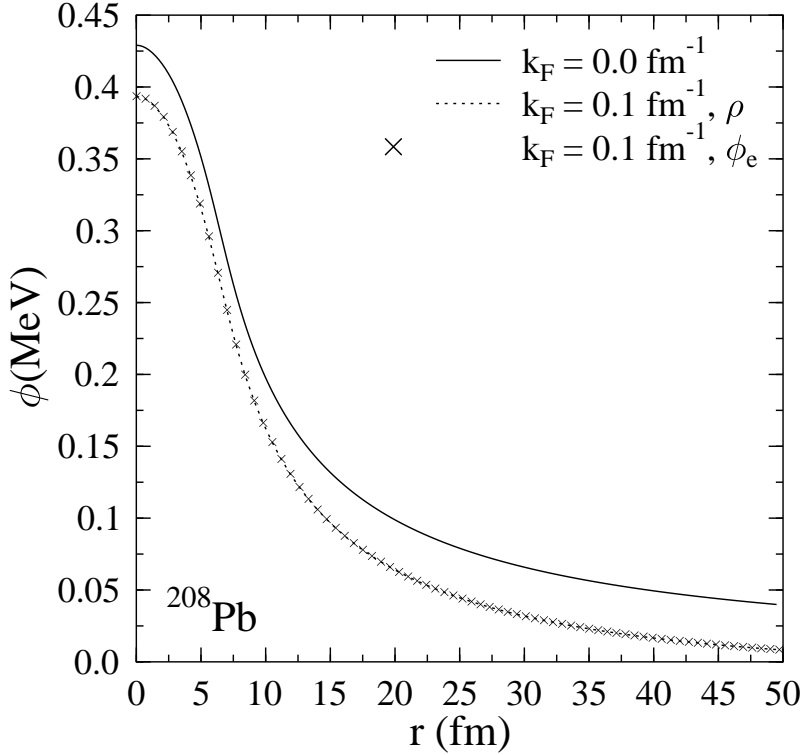


FIG. 2: The electrostatic potential ϕ shown for the doubly-magic lead nucleus for the cases of no electrons, for the inclusion of the electron density (ρ) and for the inclusion of the external electron potential (ϕ_e), respectively, at $k_F = 0.1 \text{ fm}^{-1}$.

employed as an external potential, Eq. (2.9). This interaction energy can be easily calculated for the case when the (spherical) electron and proton charge distributions are replaced by step-functions:

$$\rho_e(r) = \rho_{e0} \theta(R_C - r), \quad \rho_p(r) = \rho_{p0} \theta(R_A - r) \quad (2.11)$$

where R_C and R_A are the cell radius and nuclear radius, respectively. An elementary calculation yields for the total electrostatic energy of the cell

$$E_{Coul} = \frac{3}{5} \frac{Z^2 e^2}{4\pi R_A} c\left(\frac{\rho_{e0}}{\rho_{p0}}\right), \quad c(x) = 1 - \frac{3}{2}x^{1/3} + \frac{1}{2}x \quad (2.12)$$

This expression has the correct behavior at $x \rightarrow 0$, when it goes to the Coulomb energy of an isolated nucleus, and at $x \rightarrow 1$, when it gives zero (electron and proton charges fully compensate each other). One can see that the Coulomb energy of the nucleus is screened by the electrons. This screening effect is very significant even at moderate electron densities.

For instance, at $x = 10^{-3}$ ($k_F \approx 25$ MeV) the screening effect is about 15%. As we shall see below, this change should lead to important modifications of the decay channels involving charged particles, such as α -decay and fission.

The influence of the spherical electron cloud on the self-consistent proton potential is demonstrated in Fig. 3 for ^{208}Pb . We note that this nucleus, in the presence of electrons, is not stable anymore and would undergo electron capture. It is displayed here to demonstrate the effect of the attractive interaction between electrons and protons. The electron background leads to a downward shift of the potential but its structure remains basically unchanged within the nuclear volume. However, the principle difference from the pure Coulombic potential is evident at larger distances where the electric potential reaches zero (and zero derivative) at the boundary of the Wigner-Seitz cell. This is clearly seen in Fig. 3 for $k_F = 0.5 \text{ fm}^{-1}$ and the cell radius $R_C = 16.7 \text{ fm}$. This behavior is a result of the charge-neutrality condition which makes the electric field vanish outside the cell. We can conclude that at fixed Z and N the nuclear structure, in particular the single-particle level spacings, remains to good approximation unaltered by the presence of the electrons. As an example, we note that the proton rms radius in the heavy nucleus ^{240}Pu decreases by approximately 0.5% when adding electrons with $k_F = 0.5 \text{ fm}^{-1}$.

The Fermi energy of the protons also experiences a shift downward equal to the amount given by the additional electric potential. The neutron single-particle properties are only minimally altered, as is expected. The proton single-particle levels of ^{208}Pb are shown in Fig. 4 for $k_F = 0.0 \text{ fm}^{-1}$ and $k_F = 0.5 \text{ fm}^{-1}$. The downward shift of all levels is approximately 10 MeV. We note that while the level density as such remains the same, the positioning of the levels with respect to the continuum threshold has changed. For $k_F = 0.5 \text{ fm}^{-1}$, the number of proton states which correspond to bound orbitals has increased, and the density of states close to the continuum has increased. Furthermore, the proton separation energies have become larger. These changes in the single-particle spectra could affect, for example, nuclear reactions, in particular electron and neutron capture rates.

The total charge density for the doubly-magic lead nucleus embedded in an electron gas is displayed in Fig. 5. The negative contribution due to the electrons and the downward shift in the interior of the nucleus are clearly visible.

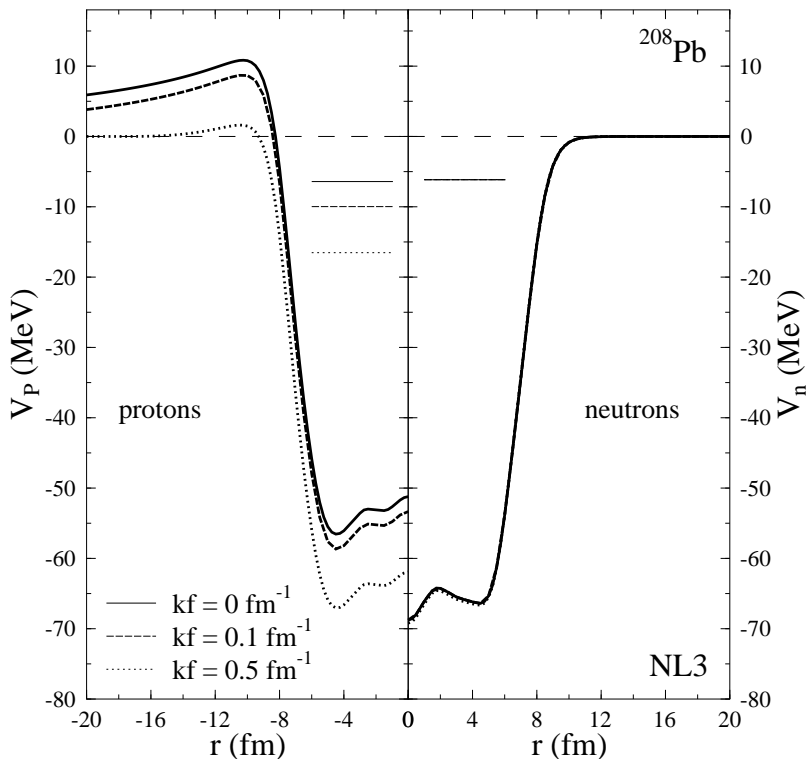


FIG. 3: The proton (left) and neutron (right) single-particle potentials in ^{208}Pb for various electron Fermi momenta. The proton and neutron Fermi energies are shown as horizontal bars

2. The deformed cell

For spherical nuclei the spherical shape of the WS cell is the obvious choice. In this case, the electric field and its derivative vanish on the cell boundary so that different cells do not experience Coulomb interactions. However, when we investigate deformed nuclei, there are several possibilities of dealing with such a situation. One possibility is to employ again a spherical WS cell, with the deformed nucleus sitting in its center. This again corresponds to a constant electron background that is not affected very much by the presence of the nucleus. However, due to the deformed proton distribution, the quadrupole moment of the whole cell is nonzero in this case. This means that the neighboring cells will experience quadrupole-quadrupole interactions. We think that for the description of deformed nuclei it is more reasonable to use deformed cells too. Therefore, we consider axially deformed spheroidal cells with the excentricity determined by the condition of vanishing quadrupole

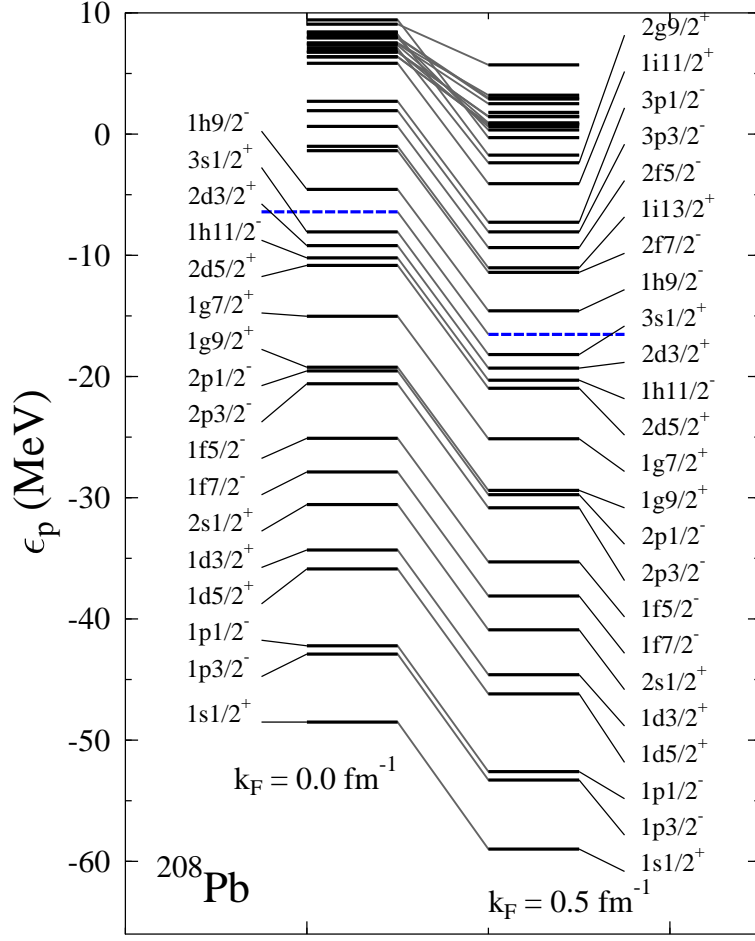


FIG. 4: (COLOR ONLINE): The proton single particle levels for $k_F = 0.0 \text{ fm}^{-1}$ (left) $k_F = 0.5 \text{ fm}^{-1}$ (right) in ^{208}Pb . The proton Fermi energies are shown as horizontal dashed lines moment.

The quadrupole moment of a given charge distribution is defined as

$$Q_{20} = \frac{1}{2} \sqrt{\frac{5}{4\pi}} \int d^3x \rho(\vec{r}) (2z^2 - r^2) \quad (2.13)$$

In our case $\rho(\vec{r}) = \rho_p(\vec{r}) - \rho_e(\vec{r})$. Thus, we adjust the shape of the electron spheroid such that $Q_{20} \equiv 0$. For the electron Fermi momenta considered in this work the electron charge density is considerably smaller than the proton charge density at the center of the nucleus, and therefore the electron spheroid has larger axes. At the same excentricity, this would result in a larger negative quadrupole moment of the electron cloud as compared with the positive quadrupole moment of protons. Thus, to balance these two contributions, the electron spheroid must have a smaller excentricity than the proton one.

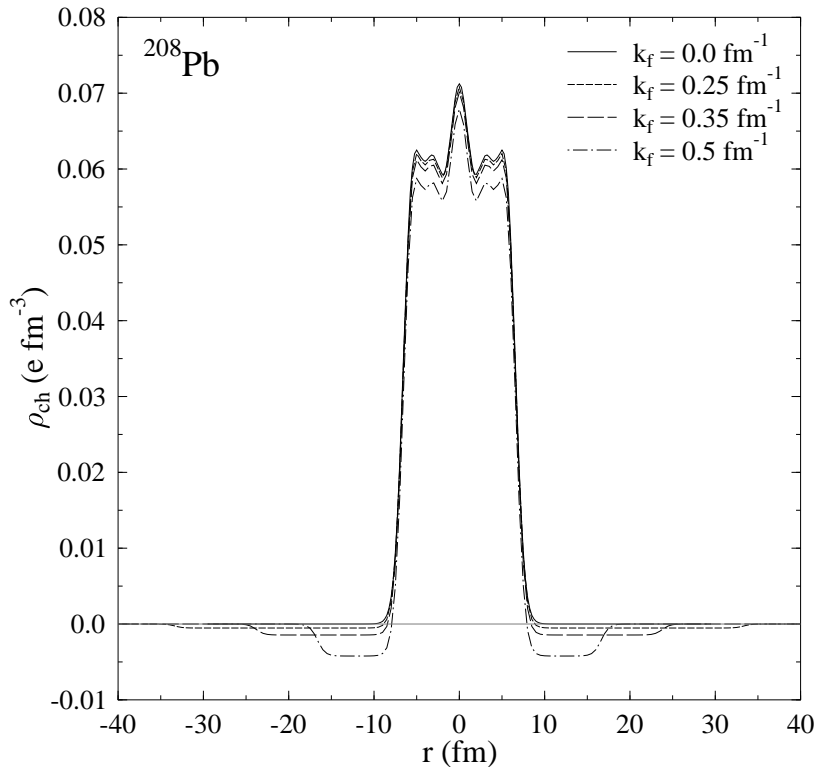


FIG. 5: The total charge density in a cell containing ^{208}Pb for various electron Fermi momenta

The realization of the deformed WS cell is illustrated in Fig. 6 for the ground state and for a largely-deformed state of ^{240}Pu . The latter shape is chosen arbitrarily to illustrate the point concerning the shape of the WS cells. At the electron Fermi momentum $k_F = 0.5 \text{ fm}^{-1}$ the equivalent spherical WS cell radius is 17.5 fm. In the ground state of Plutonium with a deformation of $\beta_2 = 0.28$, the electron cloud is almost spherical. At the deformation of $\beta_2 = 1.9$, the electron background clearly has a spheroidal shape. Still, its excentricity is much smaller than the one of the plutonium nucleus which is much more elongated. This shape corresponds to the nucleus behind the second barrier (see below). Note that this nucleus will eventually fission through the asymmetric barrier which is energetically favorable. However, the spheroidal shape used in our study can be used for axially-symmetric nuclei and, accordingly, only for symmetric fission. Generalizations of this parametrizations would involve more complicated shapes allowing also for hexadecupole and octupole degrees of freedom.

For the superheavy nucleus $^{292}120$, the corresponding charge densities are shown in Fig

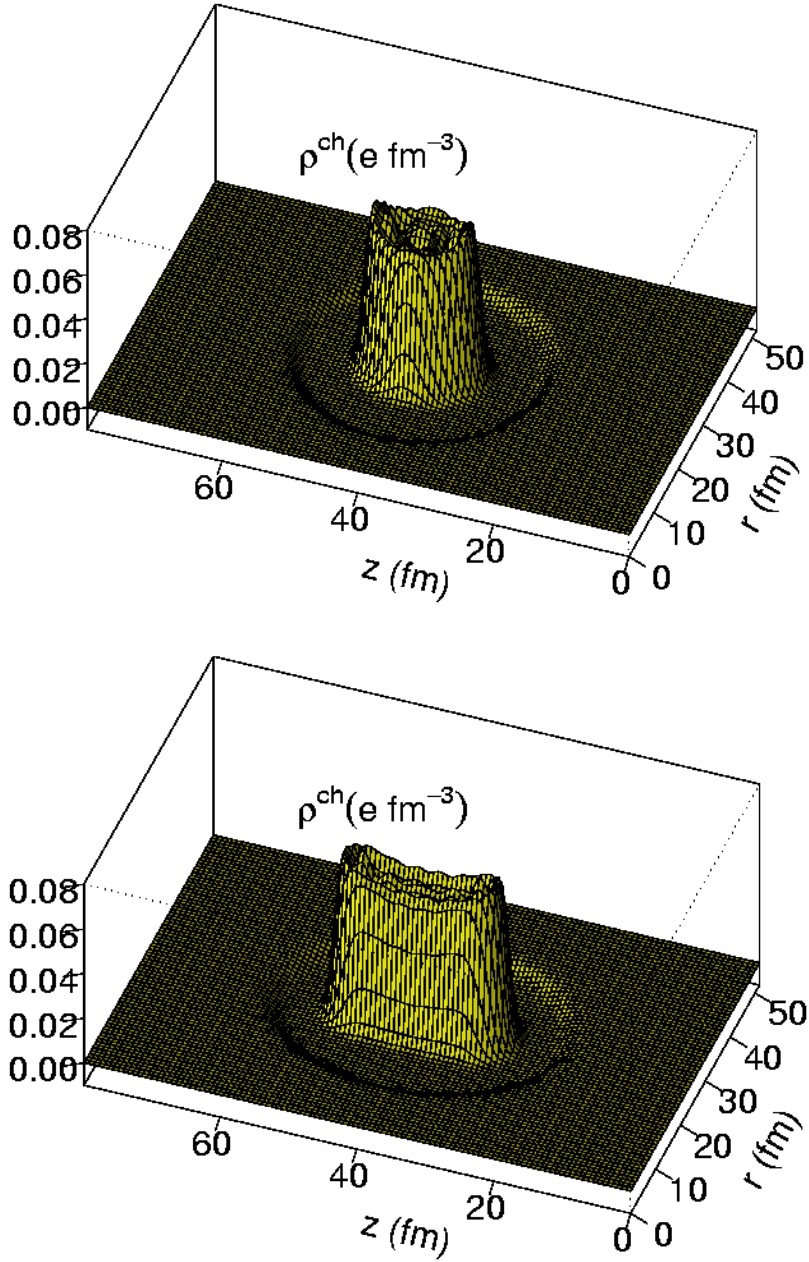


FIG. 6: (COLOR ONLINE): Total charge density of ^{240}Pu in the ground state (top) and at a deformation of $\beta_2 = 1.9$ (bottom) for electron Fermi momentum $k_F = 0.5 \text{ fm}^{-1}$

7. Again, the (spherical) ground-state and a state at large deformation are displayed. This nucleus exhibits a semi-bubble [29, 30] shape corresponding to a depletion of the baryon in its center that changes with deformation.

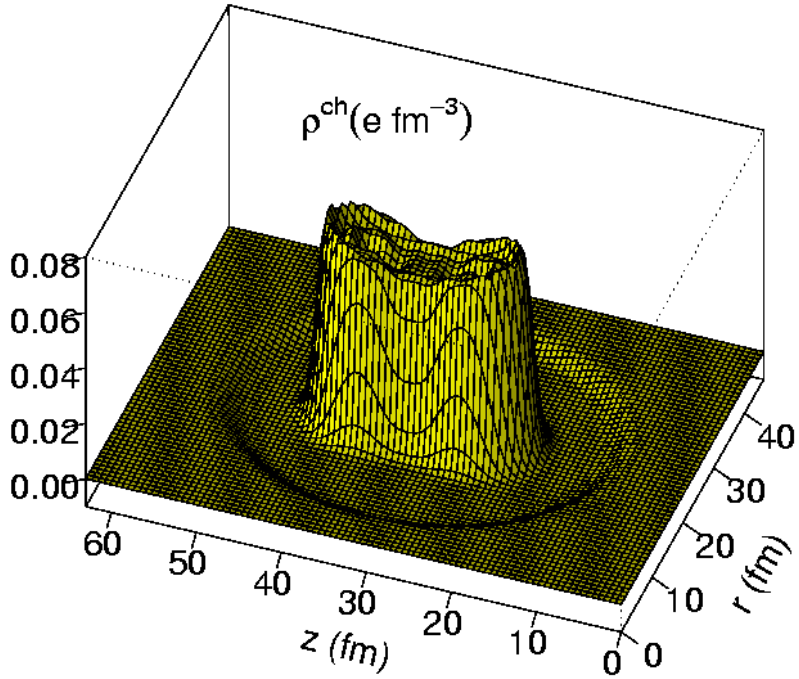
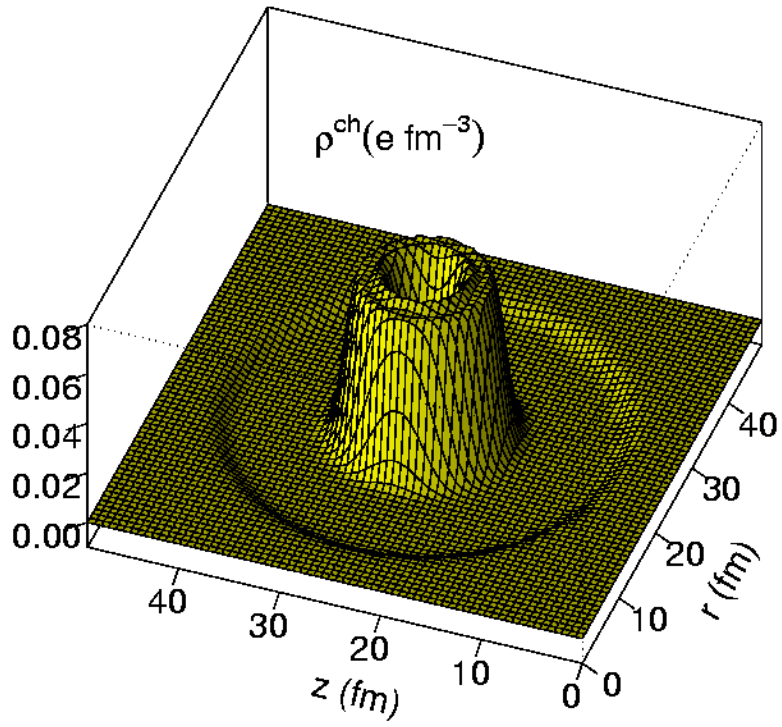


FIG. 7: (COLOR ONLINE): Total charge density of the superheavy nucleus $^{292}_{120}$ in the ground state (top) and at a deformation of $\beta_2 = 1.5$ (bottom) for electron Fermi momentum $k_F = 0.5 \text{ fm}^{-1}$

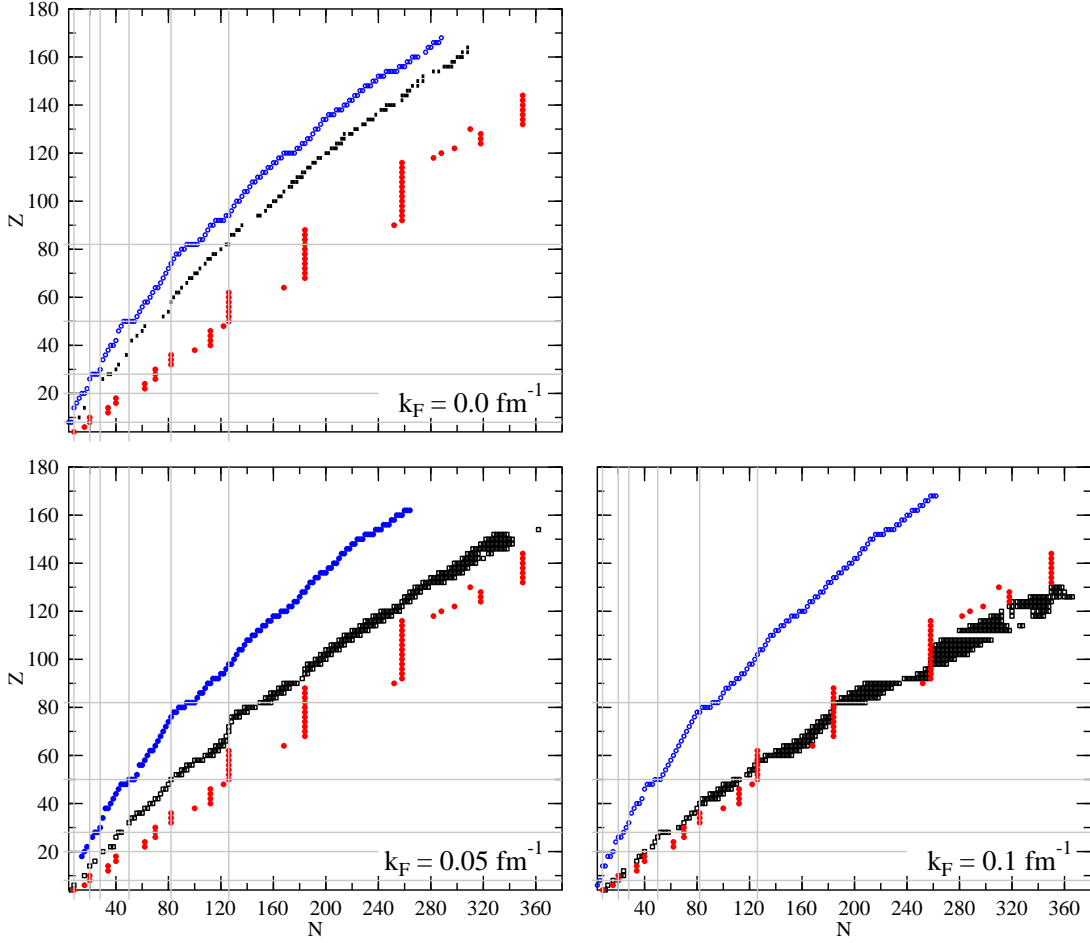


FIG. 8: (COLOR ONLINE): The line of β -stability (line in the middle, black), the proton drip-line (left-most line, blue) and the two-neutron drip-line (right-most line, red) for various electron fermi momenta. Magic numbers are indicated by grey lines.

III. NUCLEAR CHART

A. β -stability line

In this section we analyze how the nuclear β -stability valley and the proton and neutron drip lines change with increasing electron Fermi momentum. As shown before, the proton single-particle potential experiences a constant downward shift. This downward shift of the proton potential and hence the gap between proton and neutron chemical potentials is the reason for the new β -stability line. In the following, we investigate the possibility of certain decay modes of nuclei in the electron background. In particular, electron capture by nuclei

leads to a shift of the stability line to the neutron-rich side.

In the presence of electrons the equilibrium condition with respect to weak decays ($n \rightarrow p + e^- + \nu_e$, $p \rightarrow n + e^+ + \bar{\nu}_e$) reads

$$\mu_n = \mu_p + \mu_e, \quad (3.1)$$

where μ_n and μ_p are neutron and proton chemical potentials calculated within the framework of the RMF model, i.e.

$$\mu_N = \sqrt{(m_N + g_\sigma \sigma)^2 + p_{FN}^2} + g_\omega \omega^0 + g_\rho \rho^0 \tau_3, \quad N = n, p \quad (3.2)$$

The electron chemical potential is simply given by

$$\mu_e = \sqrt{k_F^2 + m_e^2} \quad (3.3)$$

where the contribution of the electrostatic potential has been neglected since it cancels out with the corresponding contribution from the proton in Eq. (3.1).

If $\mu_n > \mu_p + \mu_e$ holds, neutrons can decay into available proton states with the electron going on the top of the Fermi distribution. On the other hand, if $\mu_n < \mu_p + \mu_e$, protons can capture electrons from the Fermi distribution and occupy neutron states. Only when the condition in Eq. (3.1) is fulfilled, nuclear systems are stable with respect to these decay modes. Note that this relation becomes the well-known condition for β -stability in vacuum, $\mu_n \approx \mu_p$, for $k_F = 0$.

For zero temperature, the proton and neutron chemical potentials coincide with their Fermi energies. We note that this correspondence is not uniquely defined anymore for systems with pairing, where the effective Fermi energy is determined to yield $\langle \hat{N} \rangle = A$, but can lie somewhere between the last level contributing with nonzero occupancy and the next one. Thus, in order to obtain the (N,Z) dependence of the stability line, instead of Eq. (3.1) we employ the criterion

$$|\mu_e - (\mu_n - \mu_p)| < \Delta, \quad (3.4)$$

where $\Delta = 1$ MeV.

In Fig. 8, the β -stability lines are plotted for various values of k_F . In the same plot we show also the proton and neutron drip lines (see below). As k_F increases, the line of β -stability is shifted more and more to the neutron-rich side, i.e. the presence of electrons

stabilizes neutron-rich nuclei. This shift is so strong already for $k_F = 0.1 fm^{-1}$ that β -stability is reached only in the region of the two-neutron drip line. This means that the β -equilibrium is reached only when free neutrons appear in the system.

B. Proton- and neutron drip lines

The neutron and proton drip lines are defined by the conditions $\mu_p = m_p$ and $\mu_n = m_n$, respectively. It is clear that these nuclei are unstable with respect to weak decays so that the condition of β -equilibrium, Eq. (3.1), does not hold. In finite systems the dip lines can be defined in terms of separation energies $S_p = B(N, Z) - B(N, Z - 1)$ and $S_n = B(N, Z) - B(N - 1, Z)$. Since in this work we are only calculating even-even system, we will consider instead two-proton and two-neutron drip lines. The two-proton drip-line is defined as the position where the two-proton separation energy, defined as

$$S_{2p}(N, Z) = B(N, Z) - B(N, Z - 2), \quad (3.5)$$

goes from positive to negative values. As an approximate relation, the single-proton separation energies $S_p(N, Z)$ are related to the two-proton separation energies by $S_{2p}(N, Z) \approx 2 \cdot S_p(N, Z)$. The neutron drip line is the same for all cases shown in Fig. 8 since its position is not affected by the presence of the electrons. This follows from the fact that the neutron single-particle potential is not affected by the changes in the proton potential. Thus the neutron single-particle states are (almost completely) identical in all cases and the neutron drip line does not change. However, the results on the neutron drip line need to be taken with a grain of salt. Firstly, the calculations here are performed in spherical symmetry and deformation effects will wash out some of the strong shell effects appearing in these calculations. Secondly, we employ BCS pairing which overestimates the coupling to continuum states and the pairing contribution of the loosely bound orbitals. For nuclei close to or at the neutron drip line, full Hartree-Fock-Bogolyubov calculations should be performed. However, since here we are not interested in the precise details of the position of the neutron drip line, the BCS calculations can give us useful information on the relation between the line of β stability and the neutron drip region.

The evolution of the proton drip-line as a function of the Fermi momentum is – in addition to Fig. 8 – displayed separately in Fig. 9. As expected, this drip line shifts to more

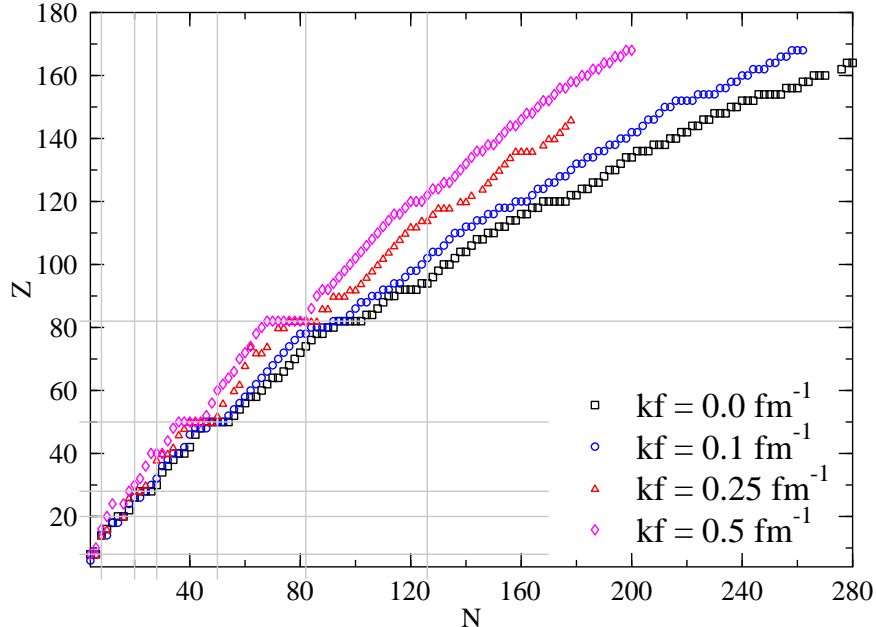


FIG. 9: (COLOR ONLINE): The proton drip-line for various electron Fermi momenta. Magic numbers are indicated by grey lines.

proton-rich nuclei as the electron Fermi momentum increases due to the additional binding of protons produced by the electron background. It is interesting that for $k_F = 0.5 \text{ fm}^{-1}$, the proton drip line is very close to the $N = Z$ condition. We can summarize our findings by stating that the region of nuclei between the conditions of proton drip and β stability has increased.

IV. DECAY MODES

A. α -decay

In this section we investigate the influence of the electron background on α -decay of nuclei. The Q_α value of the reaction is defined as

$$Q_\alpha(N, Z) = B(N, Z) - B(N - 2, Z - 2) - B(2, 2) \quad (4.1)$$

and corresponds approximately, neglecting nuclear recoil, to the kinetic energy of the α particle leaving the nucleus. In the considered environment, the binding energies of mother and daughter nuclei as well as the binding energy of the α -particle are increased due to

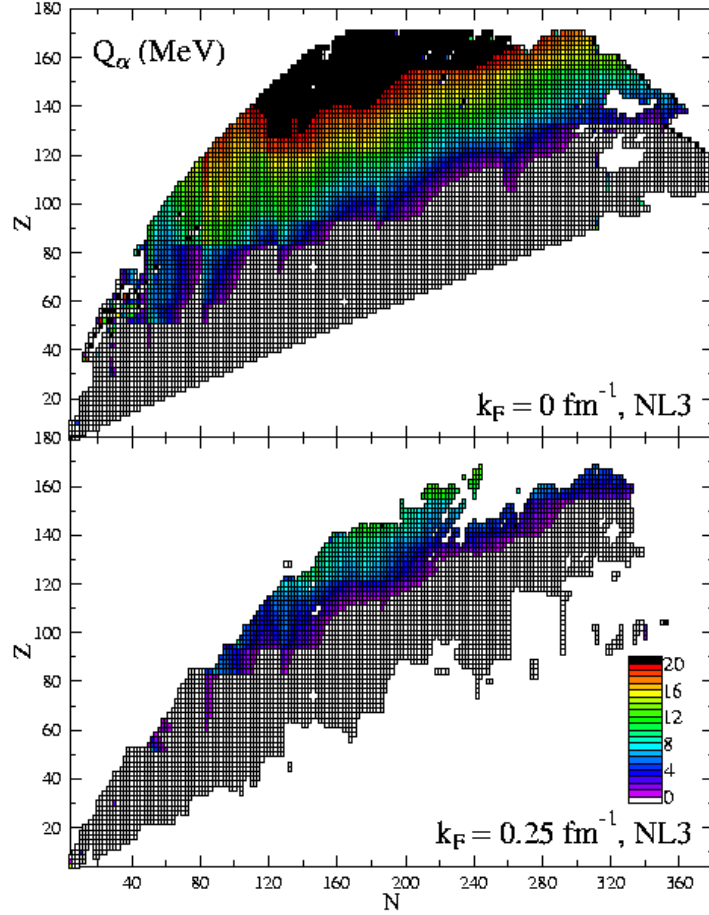


FIG. 10: (COLOR ONLINE): Q_α -values for $k_F = 0 \text{ fm}^{-1}$ (top) and $k_F = 0.25 \text{ fm}^{-1}$ (bottom). The lower boundary corresponds to $Q_\alpha = 0$. Nuclei for which no convergent solution has been achieved have been left out.

the attractive electromagnetic interaction of protons with the electron background. Fig. 10 demonstrates this effect. One can see that the overall trend is that the Q_α values decrease. Also, the boundary for which $Q_\alpha = 0$ shifts to more proton-rich nuclei. For $Q_\alpha < 0$, α -decay is not possible anymore and these systems are completely stabilized with respect to this decay mode.

The calculation of the α -decay lifetimes in the presence of electrons is not completely trivial. There are two competing effects. As seen above, the Q_α value is lowered due to the increased nuclear binding caused by electrons, which alone (for the same barrier) could increase the lifetime. We have also seen that the presence of the electrons leads to screening and modification of the Coulomb potential, see Eq. (2.12). Therefore, we need also to take

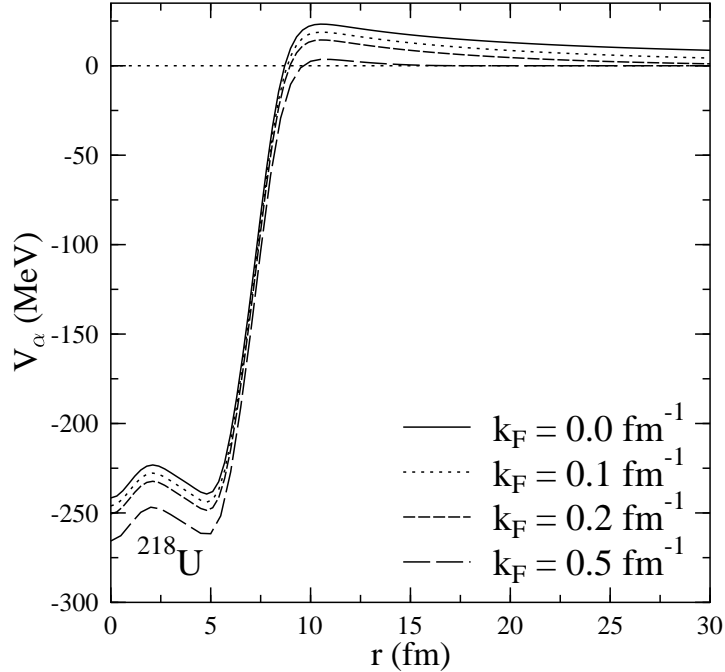


FIG. 11: α -potential for α -decay of the nucleus ^{218}U .

into account the change of the barrier through which the α particle has to penetrate. To quantify this effect we use a simple one-parameter model of Ref. [31] which expresses the α -particle potential V_α as

$$V_\alpha = 2 V_p + 2 V_n, \quad (4.2)$$

where V_p and V_n are, respectively, proton and neutron single-particle potentials. The α particle is treated as a boson. The half-life is written as $\tau_{1/2} = \ln 2/\lambda$, where the decay constant λ is parametrized as $\lambda = c P$. Here the pre-formation factor and the knocking frequency in the Gamov picture are absorbed into one parameter c , which is adjusted to known data ¹. The probability for transmission through the barrier, $P = e^S$, is calculated within the WKB approximation

$$S = -2 \int_{R_1}^{R_2} dr \sqrt{\frac{2\mu[V_\alpha(r) - Q_\alpha]}{\hbar^2}}, \quad (4.3)$$

where R_1 and R_2 are the turning points of the barrier.

As demonstrated in Ref. [31], this model performs better than the 4-parameter Viola-Seaborg systematics and additionally incorporates isovector trends, i.e. the α lifetime for

¹ A model variant that computes the knocking frequency numerically [31] yields quite similar results.

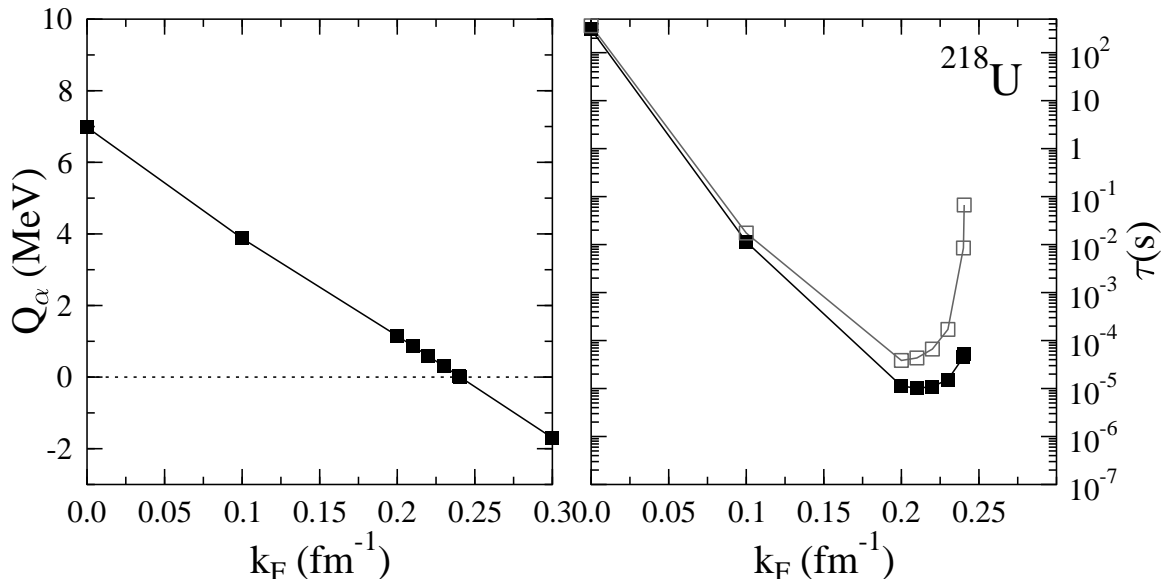


FIG. 12: The evolution of Q_α values (left) and α decay half-lives (right) for the nucleus ^{218}U as a function of the electron Fermi momentum. In the right panel, the full squares correspond to calculations within the model of Ref. [31], and open squares give results for life times multiplied with the prefactor of Eq. (4.6). The lines are drawn to guide the eye

a nucleus with given charge number possesses a dependence on the neutron number due to the self-consistent interrelation between proton and neutron single-particle potentials.

We employ this model here also for finite electron density where the potentials and the Q_α values are taken from the RMF calculations in the electron background. As an example we present results for the nucleus ^{218}U with the magic neutron number $N = 126$. We have checked in axially-symmetric calculations that both this nucleus as well as its daughter are spherical, thus no deformation effects enter the results on α -decay.

As seen in Fig. 11, the α -particle potential is lowered as a function of increasing electron Fermi momentum, making it easier for the α particle to escape the nucleus. Together with the Q_α value this leads to an overall decreasing of α half lives, see Fig 12. This holds true at low electron densities. However, this trend changes in the vicinity of the point where the Q_α values turn negative at some electron Fermi momentum k_F . At $k_F > k_F^{crit}$, α -decay becomes forbidden and nuclei are stable with respect to this decay mode. In the Uranium isotope discussed here, $k_F^{crit} = 0.24 \text{ fm}^{-1}$. However, the potential barrier experienced by the α particle at $k_F^{crit} = 0.24 \text{ fm}^{-1}$ is still ≈ 13 MeV high. If the barrier would result from

a pure nuclear charge, the lifetime for $Q_\alpha \approx 0$ would increase by a huge amount compared to situations with a finite Q_α value. The reason is that in vacuum the Coulomb barrier goes to zero asymptotically as $1/r$, thus at $Q_\alpha \approx 0$ the integration distance for the WKB formula is very large. By using a Taylor expansion of the Gamov factor for a $1/r$ potential one can find the approximate relation $\ln \tau_{1/2} \approx Q_\alpha^{-1/2}$, which leads to an infinite lifetime at $Q_\alpha \rightarrow 0$. In the case of electron background, however, the Coulomb potential is fully screened for distances larger than the Wigner-Seitz radius, which decreases with increasing electron Fermi momentum. Thus, this approximate relation is not applicable anymore. We expect that the WKB-based calculation underestimates the upwards trend shown in Fig. 12 (right), since close to the threshold this method is not accurate [32].

This situation can be illustrated by a text-book 1-D tunneling problem. A particle coming from the negative x direction encounters a rectangular barrier of height V between $x = 0$ and $x = d$. It can be shown [33] that the transmission coefficient T is given by

$$T = \left[1 + \frac{V^2}{V^2 - (2E - V)^2} \sinh^2 \left(\frac{\sqrt{2m(V - E)}d}{\hbar} \right) \right]^{-1} \quad (4.4)$$

where E and m are the energy and the mass of the tunneling particle, respectively. For typical cases of $E \approx V/2$ and $\sqrt{2m(V - E)}d/\hbar \gg 1$ (corresponding to a broad barrier compared to the de Broglie wave length of the tunneling particle), we have $\sinh(\sqrt{2m(V - E)}d/\hbar) \approx (1/4) \exp(2\sqrt{2m(V - E)}d/\hbar) \gg 1$. Since the pre-exponential is of order 1, we can neglect the first term in brackets of Eq. (4.4) and obtain

$$T \approx \exp[-2/\hbar \sqrt{2m(V - E)}d] \quad (4.5)$$

This is exactly what follows from the WKB approximation of Eq. (4.3). For electron Fermi momenta close to k_F^{crit} , however, we have $E \rightarrow 0$, and hence the prefactor diverges, i.e.,

$$\frac{V^2}{V^2 - (2E - V)^2} \approx \frac{V}{4E} \rightarrow \infty, \quad E \rightarrow 0 \quad (4.6)$$

This gives additional suppression of the tunneling probability as compared to the one obtained in the WKB approximation. Thus, the trend to longer lifetimes can be expected to set in for even smaller values of k_F compared to our calculations using the WKB approximation (Fig. 12, full squares). This means that there is a k_F^{min} for which the lifetime reaches its minimum, and for $k_F > k_F^{min}$ the lifetimes increases until the nucleus becomes stable with respect to this decay mode for $k_F \geq k_F^{crit}$. To illustrate the trend we have made

estimates of the lifetimes obtained by multiplying Eq. (4.5) with the prefactor of Eq. (4.6) for $E = Q_\alpha$. Results are shown in the right part of Fig. 12 with open squares. In this case the reversal of the downward trend in half lives occurs earlier and more dramatically compared to the previous calculations. For the electron Fermi momentum $k_F = 0.1 \text{ fm}^{-1}$ the prefactor has the value 1.53, while for $k_F = 0.2405 \text{ fm}^{-1}$ it reaches the value 1255. A further modification would arise from the fact that the exponential function in Eq. (4.4) would have to be replaced by the sinh function of Eq. (4.5) which could yield even more stabilization with respect to α decay.

The linear decrease of the Q_α values shown in Fig. 12 can be understood if we consider the electric potential caused by a spherical electron cloud given in Eq. 2.10. The potential energy V_{pot} of a point charge located in the middle of the cloud is inversely proportional to the WS cell radius R_C . Taking into account that $R_C \propto 1/k_F$, Eq. 2.6, we obtain $V_{pot} \propto k_F$, i.e., a point-like nucleus gains potential energy proportional to k_F . If Z denotes the charge number of the mother nucleus and Z_1 and Z_2 denote the charge numbers of the daughter products ($Z_1 = 2$ and $Z_2 = Z - 2$ for α decay), The change in the Q value stemming from the additional binding due to the electron cloud is given by

$$\delta Q = \frac{-3}{8\pi} \left(\frac{4}{9\pi}\right)^{1/3} e^2 k_F [Z^{5/3} - Z_1^{5/3} - Z_2^{5/3}] \quad (4.7)$$

Thus the Q_α value which depends on the energies of the mother and daughter nuclei, decreases linearly with k_F . We also see that since $Q \propto Z^{5/3}$ the largest contribution is coming from the mother nucleus.

B. Spontaneous fission

1. Deformed calculations

In order to investigate the influence of the electron background on the fission barrier of heavy and superheavy nuclei, we compute the energy of the system as a function of deformation. The cuts through the potential energy surface (PES) are calculated in axial symmetry for reflection-symmetric shapes using a constraint on the total quadrupole moment Q_{20} of the nucleus. This is achieved by adding $-\lambda \hat{Q}_{20}$ to the Hamilton operator and minimizing $\langle \hat{H} - \lambda \hat{Q}_{20} \rangle$. All other multipole moments that are allowed by the symmetry of the calculation are not constrained and adjust themselves to the solution of minimal energy. So, in

contrast to the macroscopic-microscopic approach [34], we are not operating in a limited deformation space. On the other hand, we are not necessarily exactly following the gradient in the multidimensional PES which would only be the case if the fission valley would be parallel to the Q_{20} direction [35].

At each quadrupole deformation along the fission barrier, the electron clouds excentricity and spatial extension is iteratively adjusted to match two constraints: 1) the total charge of the deformed WS cell has to be zero, and 2) the quadrupole moment of its charge distribution (including contributions from both protons and electrons) should vanish. These two constraints can be realized by varying two parameters characterizing the electron cloud, for example the lengths of long half-axis and the excentricity. As discussed above, these conditions minimize the mutual interactions of WS cells.

2. *Fission barriers*

In fission studies an important role is played by the energy of the system as a function of the deformation parameter β_2 . Our analysis shows that the shape of the electron cloud has some effect on the energy. While the spherical cloud does not produce any changes, the deformed cloud leads to visible effects.

Important key quantities related to fission are the width and the height of the fission barrier. The influence of the electrons on the fission barrier is a macroscopic effect resulting from interaction of the protons with the Coulomb potential produced by the electrons. The electrostatic repulsion between the protons is weakened by the presence of the negative charge background. This change leads to the increase of barrier height and isomer energy. Physically speaking, the electron background tends to slightly stabilize the system with respect to symmetric spontaneous fission and to increase the excitation energy of the isomeric state. We expect that asymmetric fission will be altered in a similar way, although our consideration does not allow octupole shapes. We note that the potential energy surface is determined by the dependence of the energy on the deformation. Especially for superheavy systems, the liquid drop barrier vanishes, and their stabilization results from shell effects.

The trends discussed above are clearly seen in Fig. 13 which displays the fission barrier of Plutonium for different choices of the electron density in the spheroidal configuration. The inner barrier increases with increasing k_F leading to a stabilization effect towards sponta-

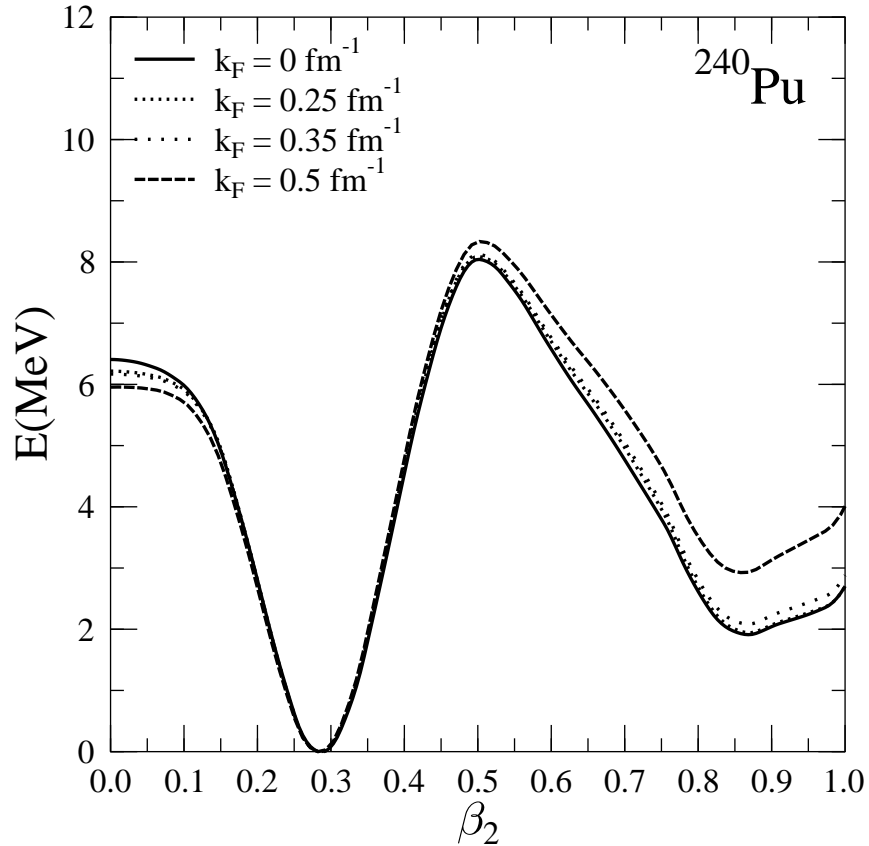


FIG. 13: Fission barrier of ^{240}Pu for various electron densities in spheroidal configurations.

neous fission. Furtheron, the properties of the shape isomer (second minimum) are altered due to the electrons background too. For $k_F = 0.5 \text{ fm}^{-1}$ we see an increase of the inner fission barrier by approx. 0.3 MeV and the energy of the isomeric state increases by approximately 1 MeV. Note that the ground-state binding energy of ^{240}Pu with NL3 is 1814 MeV, the presence of the electrons increases it to the value of 2248 MeV (the latter does not include the kinetic energy of the electrons). As another example, we show the influence of the electron background on the fission barrier of ^{256}Fm in Fig. 14. The presence of the electrons leads to a slight increase of the first barrier. The effect is more dramatic for the isomeric state, where an increase in energy of 2 MeV is found at $k_F = 0.5 \text{ fm}^{-1}$. Note that the low energy of the second minimum, which is below the ground state, is a (unrealistic) prediction which has also been found in a systematic study for heavy and superheavy nuclei [36].

Fig. 15 demonstrates the influence of the electron background on the superheavy nucleus $^{292}120$. In this case, the electron background leads to a slight decrease of the width and

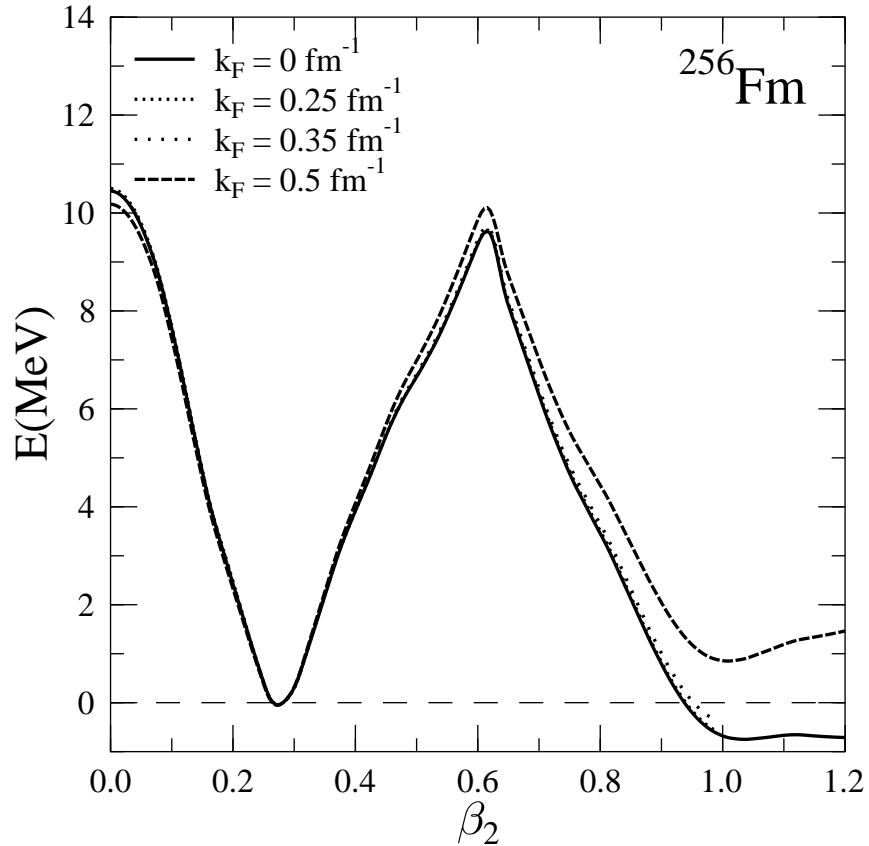


FIG. 14: Fission barrier of ^{256}Fm in for various electron densities in spheroidal configurations.

height of the inner barrier calculated with the spheroidal electron cloud. But the height of the second minimum has increased by about 0.7 MeV. Note, however, that the inclusion of reflection-asymmetric degrees of freedom in these superheavy systems make the second barrier vanish [36]. It is interesting that the potential energy surface is affected in a different way compared to the case of Plutonium. The reasons are related to the fact that the barrier starts out from a spherical minimum, and that the charge number in this nucleus is much larger so that the total contribution of the Coulomb energy to the total energy is strongly increased compared to plutonium.

We can speculate about even heavier systems. In Ref. [37], the shell corrections for super- and hyperheavy nuclei were calculated within the framework of self-consistent mean-field models. It was found that the familiar concept of strongly-pronounced magic numbers dissolves due to the high level-density, and rather a broad region of shell-stabilization can be found. We choose the hyperheavy nucleus $^{462}154$, which is located in such a region of

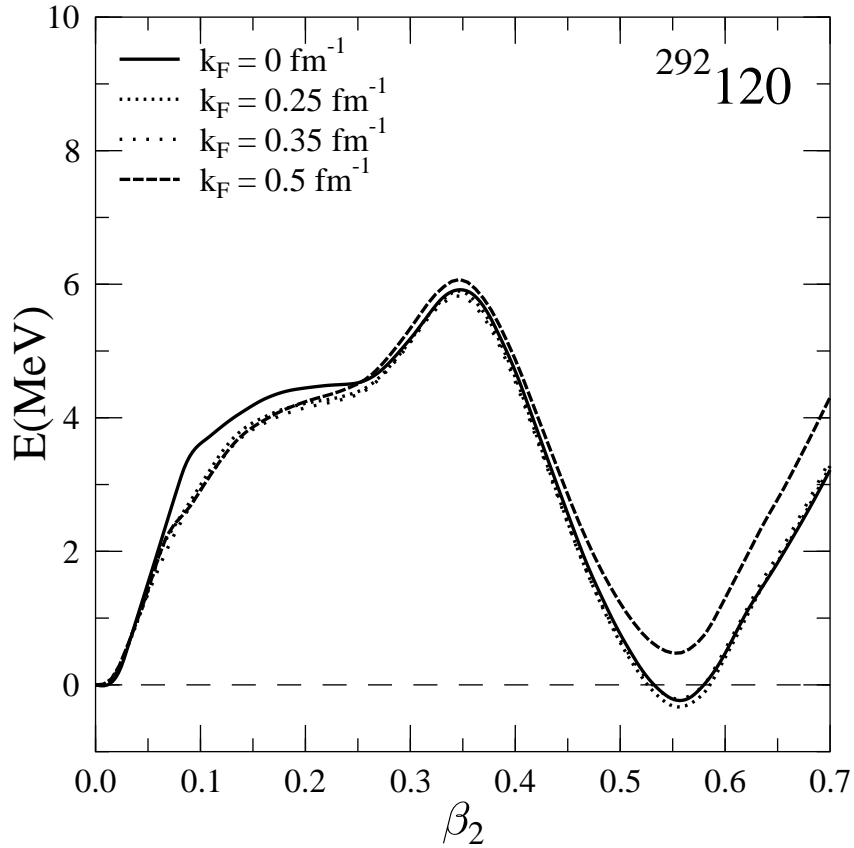


FIG. 15: Fission barrier of the superheavy nucleus $^{292}_{120}$ for various electron densities in spheroidal configurations.

shell-stabilization (for the RMF force NL3), as an example. Its fission barrier can be seen in Fig. 16. The strong shell corrections lead to a spherical minimum and to a barrier which is about 6.5 MeV high, and almost 1 MeV larger in the presence of electrons.

A word of caution is in order. For both this hyperheavy nucleus and the superheavy system $^{292}_{120}$ discussed before, the calculation of the axial barrier gives us only partial information on the principal impact of the electron background on the fission barrier. The actual fission path, however, might deviate quite strongly from this path, and for these heavy systems fissioning through the triaxial plane is rather probable.

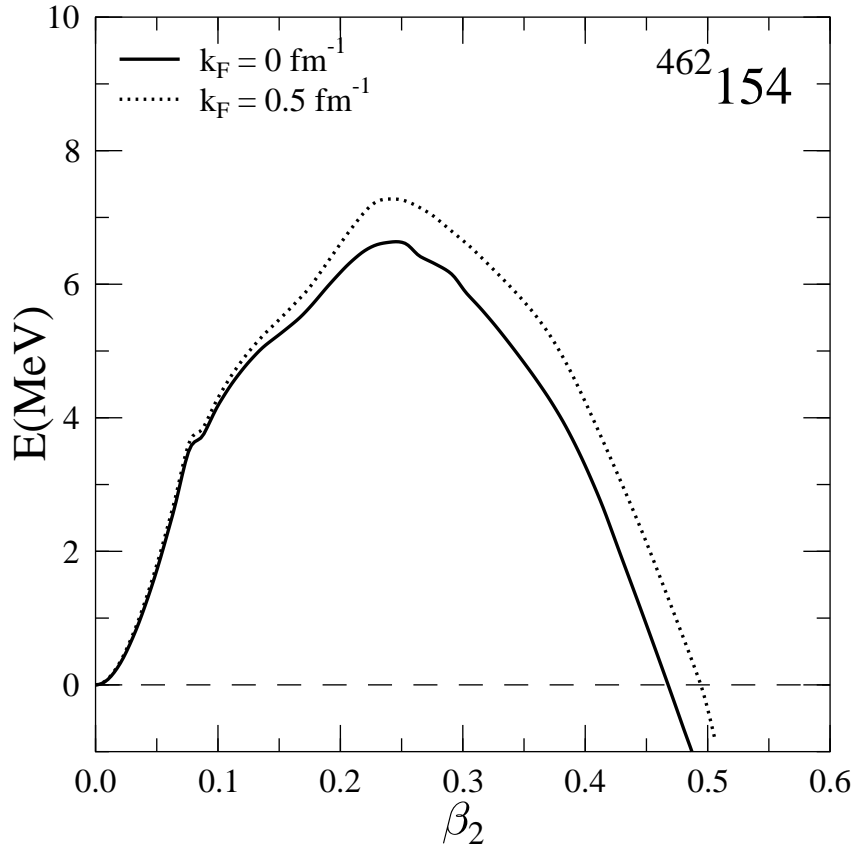


FIG. 16: Fission barrier of the superheavy nucleus $^{462}_{154}$ without electrons and for $k_F = 0.5 \text{ fm}^{-1}$

3. Fission Q values

As discussed in Section II B 1, due to the screening of the electrons the Coulomb energy of nuclei is lowered as compared with the vacuum case. This will lead to the reduction of the Q value for spontaneous fission, in full analogy to the case of α decay. Fig. 17 shows the Q value for symmetric fission of ^{256}Fm as a function of the electron Fermi momentum. One can clearly see this trend and we think it will be present for asymmetric fission too. To evaluate the fission probability one should perform detailed calculations of the fission barrier for the case of a two-center nuclear shape. This work is in progress now. At this stage we can only point out that due to the screening of the Coulomb potential the fission barrier is altered and the Q value will decrease. We expect that the latter trend is more important so that the net effect is suppression of spontaneous fission. This follows also from simple

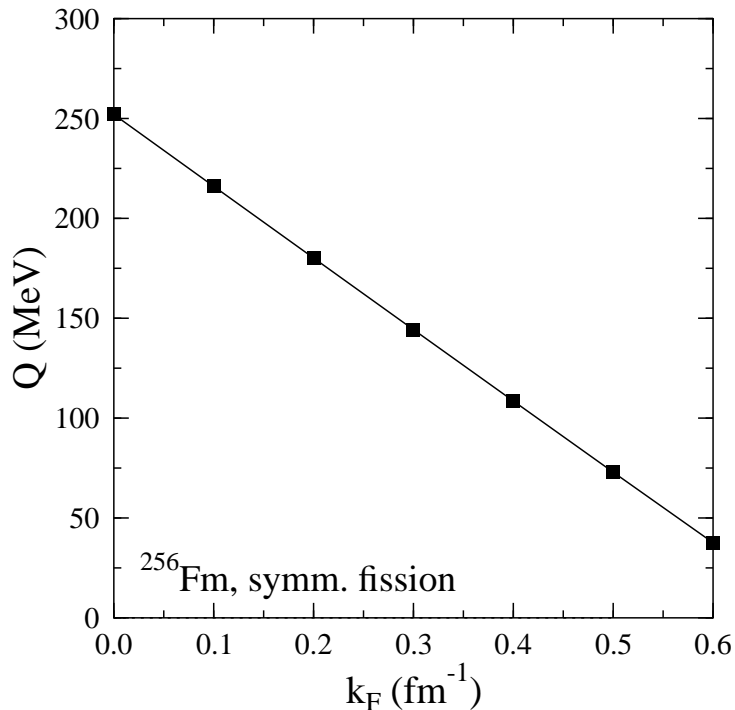


FIG. 17: Q value for symmetric fission of ^{256}Fm as a function of the electron Fermi momentum k_F .

estimates based on the liquid-drop model. Indeed, let us consider the fissility parameter

$$\frac{Z^2}{A} = \frac{2a_S}{a_C}, \quad (4.8)$$

where $a_S \approx 18 \text{ MeV}$ and $a_C \approx 0.72 \text{ MeV}$ are, respectively the surface and Coulomb coefficients in the Weizsäcker formula. If we take into account the electron screening, the Coulomb energy is reduced by the factor c , Eq. (2.12). Therefore the modified fissility parameter is $\frac{Z^2}{A} = \frac{50}{c}$. Since $c(x) < 1$, this means that in the presence of electrons the region of spontaneous fission moves to heavier nuclei. For instance, for $k_F = 0.25 \text{ fm}^{-1}$, the fissility parameter is 80 instead of 50 in vacuum.

V. CONCLUSIONS AND OUTLOOK

We have studied the properties of atomic nuclei embedded in an electron gas as occurring in, e.g., neutron star crusts and supernova explosions. Nuclear structure calculations have been performed within the relativistic mean-field approach employing the force NL3. The

calculations have been performed within the Wigner Seitz cell approximation in coordinate-space. A fermi-type distribution with a smooth surface has been employed in order to get rid of artifacts stemming from the discrete grid spacing. For spherical systems, a spherical Wigner-Seitz cell has been used. We have discussed an implementation of spheroidal Wigner-Seitz cells for axially-deformed nuclei. We employ the criterion that in addition to the total charge also the total electric quadrupole moment of a cell should vanish. This leads to an iteratively self-adjusting Wigner-Seitz cell for each given deformation of the nucleus.

The presence of electrons leads to effects which have rather macroscopic character. We did not find any significant changes in the single-particle levels regarding their relative positions. Since the electron background is constant over the nuclear volume – by construction – it leads predominantly to a constant downward shift of the proton potential.

The electron gas alters the stability condition for β decay and shifts the stability line to more neutron-rich nuclei. Electron capture becomes a relevant process, the transformation of protons into neutrons favors large isospin in nuclei. Furthermore, the two-proton dripline is shifted to more proton-rich nuclei since the protons gain additional binding due to the attractive interaction with the electrons. The neutron drip line is not altered by the presence of the electrons since the neutron single-particle potential remains (to a very good approximation) unaffected.

We have found that in a dense electron background decay modes such as α -decay and spontaneous fission are suppressed. Our calculations show that the α decay half lives decrease as a function of the electron Fermi momentum k_F until they get stabilized for larger k_F . A general trend is that the Q values of those decay modes decrease with increasing electron density.

We have also calculated the potential energy surface as a function of the electron Fermi momentum within the framework of the self-adjusting axial Wigner Seitz cell. We have found that only for very large electron Fermi momenta a change is occurring for the inner axial barrier and the energetic position of the isomeric state. This could hint again at stabilization of the fission mode for high electron densities.

Overall, the electron gas broadens the part of the nuclear chart lying between the proton drip line and the valley of β - stability. Stabilizing effects with respect to α decay and spontaneous fission occur for large electron Fermi momenta. Hence, in extreme astrophysical environments, the production of very exotic and superheavy nuclei could become possible.

This might happen during the r-process (rapid neutron capture) and the rp-process (rapid proton capture) when the electron background prevents the heavy (and superheavy) nuclei from fast decay by spontaneous fission or alpha decay. As a consequence, the nuclei, which otherwise would be unstable, can provide a bridge to the island of superheavy elements. We are planning to study this possibility in the future. If long-lived or even stable superheavy nuclei exist, they could be created in such an environment and later ejected into space. Then one can try to search for such superheavy nuclei in cosmic rays. Another natural step in our investigations is to add free neutrons and study nuclei in the environment of free electrons and neutrons. Work in this direction is in progress.

Acknowledgement

Fruitful discussions with J. A. Maruhn, S. Reddy, P.-G. Reinhard, N. Sandulescu, L. Satarov, J. Schaffner-Bielich and S. Schramm are gratefully acknowledged. This work was supported in part by the Gesellschaft für Schwerionenforschung (Germany) and by grants RFFR-02-04013 and NS-8756.2006.2 (Russia).

Appendix

A. Role of Coulomb exchange

In relativistic models such as used in this study, the Coulomb interaction is usually calculated within the Hartree approximation, i.e.

$$\mathcal{E}_{Coulomb}^{dir} = e^2 \frac{1}{2} \int \int d^3r d^3r' \frac{\rho_p(\vec{r}) \rho_p(\vec{r}')}{|\vec{r} - \vec{r}'|} \quad (5.1)$$

where $\rho_p(\vec{r})$ is the proton density. This relates to the fact that the RMF model traditionally is formulated as a Hartree theory, and no explicit exchange terms in the effective nucleon-nucleon interaction are taken into account. In contrast to effective field theories with contact interactions, exchange terms involving finite-range meson fields are computationally expensive, and so far no significant improvement over Hartree-like formulations has been achieved. The role of 4-fermion interactions has been studied in Ref. [38] for the point-coupling variant of the RMF model, the RMF-PC model. It has been found that, while the formal structure of the model remains the same and only a redefinition of 4-fermion coupling constants

occurs, the interpretation of the various terms becomes quite different. For higher-order point-coupling terms and derivative terms, however, the Fierz transformations [39] yield a large number of terms which do not improve the model [40].

In the Skyrme-Hartree-Fock approach, the Coulomb exchange term is usually included in Slater approximation [41]:

$$\mathcal{E}_{Coulomb}^{ex} = \frac{3}{4}e^2 \left(\frac{3}{4}\right)^{1/3} \int d^3r [\rho_p(\vec{r})]^{4/3} \quad (5.2)$$

In our calculations, we replace the proton density by the absolute value of the charge density, i.e., $\rho_p(\vec{r})$ by $|\rho_{ch}(\vec{r})| = |\rho_p(\vec{r}) + \rho_e(\vec{r})|$.

For nuclei close to stability, it can be shown that the Coulomb exchange effect can be absorbed by a refit of the mean-field parameters [42]. It remains to be seen, however, if this still holds true for exotic nuclei and nuclei close to the proton drip-line, as well as nuclear systems studied here. As demonstrated in Fig. 18, the Coulomb exchange interaction both in vacuum and at high electron chemical potential yields a rather small contribution to the potential, and Fermi energies for the two cases differ by 0.4 MeV only. Thus the properties of nuclei in an electron gas are not sensitive to the exclusion or inclusion of (Slater-) Coulomb exchange in the calculation.

-
- [1] R.A. Alpher, H. Bethe, G. Gamow, *Phys. Rev.* **73** (1948) 803.
 - [2] Yong-Zong Quian, *Prog. Part. Nucl. Phys.* **50**, 153 (2003)
 - [3] H.A. Bethe, *Rev. Mod. Phys.* **62**, 801 (1990).
 - [4] H.-T. Janka, R. Buras, K. Kifonidis, M. Rampp, and T. Plewa, Review in "Core Collapse of Massive Stars", Fryer, C.L. (ed.) , *astro-ph/0212314* (2001); H.-T. Janka and E. Mueller, *Astron. Astrophys.* **306**, 167 (1996).
 - [5] M. Liebendorfer, A. Mezzacappa, O. E. B. Messer, G. Martinez-Pinedo, W. R. Hix and F. -K. Thielemann, *Nucl. Phys.* **A719**, 144c (2003)
 - [6] J.M. Lattimer, C.J. Pethick, D.G. Ravenhall and D.Q. Lamb, *Nucl. Phys.* **A432**, 646 (1985).
 - [7] J.M. Lattimer and F.D. Swesty, *Nucl. Phys.* **A535**, 331 (1991). H. Shen, H. Toki, K. Oyamatsu, and K. Samiyoshi, *Nucl. Phys. A* **637** (1998) 435. C. Ishizuka, A. Ohnishi, and K. Samiyoshi, *Nucl. Phys. A* **723** (2003) 517
 - [8] A.S. Botvina and I.N. Mishustin, *Phys. Lett.* **B584**, 233 (2004).

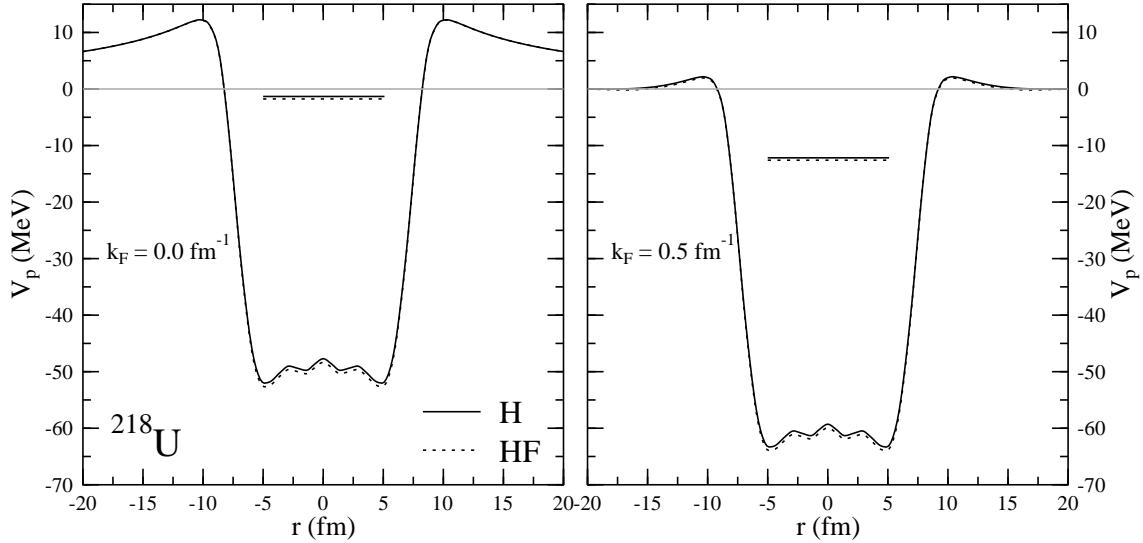


FIG. 18: The proton single-particle potential for ^{218}U in the absence of electrons (left) and for $k_F = 0.5\text{fm}^{-1}$ (right) involving only the direct Coulomb term (H) and involving both direct term and exchange term in Slater approximation (HF). Also shown are the proton fermi energies for both cases.

- [9] A.S. Botvina and I.N. Mishustin, *Phys. Rev.* **C72**, 048801 (2005).
- [10] D. G. Ravenhall, C. J. Pethiek, and J. R. Wilson, *Phys. Rev. Lett.* **50**, 2066 (1983)
- [11] C. J. Horowitz, *Eur. Phys. J.* **A30**, 303 (2006)
- [12] T. Maruyama, T. Tatsumi, D. N. Voskresenky, T. Tanigawa, S. Chiba, and T. Maruyama, nucl-th/0402002 v1
- [13] T. Maruyama, T. Tatsumi, T. Endo, and S. Chiba, nucl-th/0605075 v1
- [14] J. W. Negele, and D. Vautherin, *Nucl. Phys.* **A207** (1973) 298
- [15] P. Magierksi, A. Bulgac, and P.-H. Heenen, nucl-th/0112003 v1
- [16] P. Magierski and P.-H. Heenen, nucl-th/112018 v1
- [17] F. Douchin and P. Haensel, nucl-th/9808030 v1
- [18] N. Sandulescu, nucl-th/0403019 v2
- [19] K. S. Cheng, C. C. Yao, and Z. G. Dai, *Phys. Rev. C* **55** (1997) 2092
- [20] H. Toki, K. Sumiyoshi, D. Hirata, H. Shen, and I. Tanihata, RIKEN Revire No. 26 (2000) 17
- [21] P.-G. Reinhard, *Rep. Prog. Phys.* **52**, 439 (1989).
- [22] M. Bender, P.-H. Heenen, P.-G. Reinhard, *Rev. Mod. Phys.* **75**, 121 (2003).

- [23] B. A. Nikolaus, T. Hoch, and D. G. Madland, Phys. Rev. C **46**, 1757 (1992)
- [24] T. Bürvenich, D. G. Madland, J. A. Maruhn, and P.-G. Reinhard, Phys. Rev. C **65** (2002) 044308
- [25] T. Niksic, D. Vretenar, and P. Ring, Phys. Rev. C **72** (2005) 014312
- [26] M. Bender, K. Rutz, P.-G. Reinhard, and J. A. Maruhn, Eur. J. Phys. A **8**, 59 (2000)
- [27] G. Lalazissis, J. König, and P. Ring, Phys. Rev. C **55** (1997) 540
- [28] M. Baldo, E.E. Saperstein, S.V. Tolokonnikov, Nucl.Phys. **A775**, 235 (2006)
- [29] M. Bender, K. Rutz, P.-G. Reinhard, J. A. Maruhn, and W. Greiner, Phys.Rev. **C60** (1999) 034304
- [30] J. Decharge, J.-F. Berger, K. Dietrich, and M. S. Weiss, Phys.- Lett. **B 451** (1999) 275
- [31] Z. A Dupre and T. J. Bürvenich, Nucl. Phys. **A767**, 81 (2006)
- [32] H. K. Shepard, Phys. Rev. D **27**, 1288 (1983)
- [33] T. Mayer-Kuckuck, *Kernphysik*, 2nd Edition Stuttgart, Teubner 1980
- [34] P. Möller, J.R. Nix, W.D. Myers, and W.J. Swyatecki, At. Data Nucl. Data Tables **59**, 185 (1995)
- [35] H.Flocard, P.Quentin, A.K.Kerman and D.Vautherin, Nucl. Phys. **A203** (1973) 433
- [36] T. Buervenich, M. Bender, J. A. Maruhn, and P.-G. Reinhard Phys.Rev. **C69** (2004) 014307; Erratum-ibid. **C69** (2004) 029901
- [37] M. Bender, W. Nazarewicz, and P.-G. Reinhard, Phys. Lett. **B515** (2001) 42-48
- [38] D. G. Madland, T. J. Bürvenich, J. A. Maruhn, and P.-G. Reinhard, Nucl.Phys. A **741**, 52 (2004)
- [39] J. A. Maruhn, T. Bürvenich, and D. G. Madland, J. of. Comp. Phys. **169**, 238 (2001)
- [40] T. Cornelius, unpublished results
- [41] J. C. Slater, Phys. Rev. **81**, 385 (1951)
- [42] T. J. Bürvenich, unpublished results